JGR Space Physics

RESEARCH ARTICLE
10.1029/2021JA030238

Discrete Aurora at Mars: Dependence on Upstream Solar Wind Conditions

Z. Girazian[1], N. M. Schneider[2], Z. Milby[2], X. Fang[2], J. Halekas[1], T. Weber[3], S. K. Jain[2], J.-C. Gérard[4], L. Soret[4], J. Deighan[2], and C. O. Lee[5]

[1]Department of Physics and Astronomy, University of Iowa, Iowa City, IA, USA, [2]Laboratory for Atmospheric and Space Physics, University of Colorado Boulder, Boulder, CO, USA, [3]NASA Goddard Space Flight Center, Greenbelt, MD, USA, [4]LPAP, STAR Institute, Université de Liége, Liége, Belgium, [5]Space Sciences Laboratory, University of California, Berkeley, CA, USA

Key Points:

- Outside the strong crustal field region, high solar wind pressures increase the aurora detection frequency but not the emission brightness
- IMF orientation affects the aurora detection frequency more prominently near strong crustal fields
- In the strong crustal field region, aurora are rare when the IMF points near the radial or anti-radial directions

Correspondence to:
Z. Girazian,
zachary-girazian@uiowa.edu

Citation:
Girazian, Z., Schneider, N. M., Milby, Z., Fang, X., Halekas, J., Weber, T., et al. (2022). Discrete aurora at Mars: Dependence on upstream solar wind conditions. *Journal of Geophysical Research: Space Physics*, *127*, e2021JA030238. https://doi.org/10.1029/2021JA030238

Received 10 JAN 2022
Accepted 15 MAR 2022

Abstract Discrete aurora at Mars, characterized by their small spatial scale and tendency to form near strong crustal magnetic fields, are emissions produced by particle precipitation into the Martian upper atmosphere. Since 2014, Mars Atmosphere and Volatile EvolutioN's (MAVEN's) Imaging Ultraviolet Spectrograph (IUVS) has obtained a large collection of UV discrete aurora observations during its routine periapsis nightside limb scans. Initial analysis of these observations has shown that, near the strongest crustal magnetic fields in the southern hemisphere, the IUVS discrete aurora detection frequency is highly sensitive to the interplanetary magnetic field (IMF) clock angle. However, the role of other solar wind properties in controlling the discrete aurora detection frequency has not yet been determined. In this work, we use the IUVS discrete aurora observations, along with MAVEN observations of the upstream solar wind, to determine how the discrete aurora detection frequency varies with solar wind dynamic pressure, IMF strength, and IMF cone angle. We find that, outside of the strong crustal field region (SCFR) in the southern hemisphere, the aurora detection frequency is relatively insensitive to the IMF orientation, but significantly increases with solar wind dynamic pressure, and moderately increases with IMF strength. Interestingly however, although high solar wind dynamic pressures cause more aurora to form, they have little impact on the brightness of the auroral emissions. Alternatively, inside the SCFR, the detection frequency is only moderately dependent on the solar wind dynamic pressure, and is much more sensitive to the IMF clock and cone angles. In the SCFR, aurora are unlikely to occur when the IMF points near the radial or anti-radial directions when the cone angle ($\arccos(B_x/|B|)$) is less than 30° or between 120° and 150°. Together, these results provide the first comprehensive characterization of how upstream solar wind conditions affect the formation of discrete aurora at Mars.

1. Introduction

Discrete aurora at Mars were discovered by the Spectroscopy for Investigation of Characteristics of the Atmosphere of Mars (SPICAM) Ultraviolet (UV) spectrometer instrument on Mars Express (Bertaux et al., 2006). The first observed UV auroral emissions, detected during a nightside limb scan, emanated from a small patch of atmosphere (with a horizontal scale of ~30 km) near one of the strongest crustal magnetic field regions in the southern hemisphere. Subsequent SPICAM aurora observations indicated that these two characteristics—(1) a small spatial scale and (2) a general tendency to form near strong crustal field regions—are common features of discrete aurora (Gérard et al., 2015; Leblanc et al., 2006). These characteristics also distinguish discrete aurora from diffuse aurora and proton aurora, which are the other two types of auroras that have been observed at Mars (Deighan et al., 2018; Hughes et al., 2019; Ritter et al., 2018; Schneider et al., 2015).

UV spectra of discrete auroral emissions, also collected by the MEX UV instrument, indicate that the aurora are produced by collisional processes between precipitating electrons (which are tied to magnetic fields) and atmospheric species. Specifically, the UV aurora are observed as excess emissions in the CO Fourth positive bands between 135 and 170 nm, CO Cameron bands between 190 and 270 nm, the CO_2^+ UV doublet at 289 nm, and the excited oxygen emission line at 297.2 nm (Bertaux et al., 2005; Gérard et al., 2015; Leblanc et al., 2006; Soret et al., 2016). In total, however, the SPICAM UV instrument observed only ~20 discrete aurora, all of which were near the strongest crustal magnetic field region in the southern hemisphere of Mars.

Recently, a more comprehensive set of discrete aurora observations has been obtained by the Mars Atmosphere and Volatile EvolutioN (MAVEN) Imaging Ultraviolet Spectrograph (IUVS; Schneider et al., 2021; Soret et al., 2021). Since 2014, IUVS has gathered ~300 discrete aurora detections during routine nightside periapsis limb scans. Using this larger database of observations, Schneider et al. (2021) (hereafter Schneider21) discovered several new features of the discrete aurora. They found that, although aurora are more commonly observed near strong crustal fields (~4% detection frequency), they also can occur nearly anywhere on the planet (<1% detection frequency). Schneider21 also showed there is a peculiar local time and interplanetary magnetic field (IMF) dependence for aurora that occur near the strongest crustal magnetic field region in the southern hemisphere. Inside this region, which Schneider21 defines as a rectangle spanning 30°S−60°S in latitude and 150°E−210°E in longitude, discrete aurora are observed almost exclusively at evening local times when the IMF clock angle is negative (IMF $B_Y < 0$). This particular geometry, then, may be favorable for magnetic reconnection, which allows particles to access this region of the atmosphere and produce aurora. Interestingly, outside the strong crustal field rectangle, the discrete aurora detection frequency is only weakly dependent on local time and IMF clock angle.

The energetic electrons (hundreds of eV) that produce discrete aurora have also been observed by instruments on several spacecraft. These electrons have peaked electron energy distributions that are similar to the electron energy distributions responsible for discrete aurora at Earth (D. A. Brain et al., 2006; Leblanc et al., 2008; Gérard et al., 2015; Xu et al., 2020). They are also concentrated near crustal magnetic field cusps (D. Brain & Halekas, 2013). These "inverted-v" electron signatures at Mars suggest an analogy with Earth's auroral oval, where electrons are accelerated downward toward the open-closed magnetic field boundary (Birn et al., 2012). At Mars the process appears somewhat analogous, but the aurora are more scattered across the planet due to the more disorganized crustal magnetic fields. However, despite these similarities between Earth and Mars, the electron acceleration mechanisms at Mars are not yet fully understood (D. Brain & Halekas, 2013; Akbari et al., 2019).

In this work we use MAVEN IUVS observations to determine how the discrete aurora detection frequency varies with upstream solar wind conditions. We focus, in particular, on the solar wind dynamic pressure, IMF strength, IMF clock angle, and IMF cone angle measured contemporaneously by MAVEN instruments. Our results provide constraints for future theoretical and modeling studies aimed at understanding discrete aurora formation mechanisms.

2. Observations

2.1. Discrete Aurora

MAVEN IUVS (McClintock et al., 2015) observes discrete aurora during routine nightside periapsis limb scans. The limb scan dataset used in this work is the same as described in Schneider21, and we refer readers to that publication for a detailed description of dataset, the IUVS observing mode, and data caveats. Here we present only a brief description.

During each periapsis pass IUVS obtains 12–24 limb scans that cover a small range of latitudes, longitudes, and local times. The scans are combined to construct a two dimensional image of atmospheric UV emissions projected against the planetary limb. The UV spectra observed in each pixel are used to isolate and extract the emission brightness in the CO Cameron bands. Scans that contain a statistically robust CO Cameron band brightness are considered a discrete auroral detection. Note that the IUVS sensitivity limit in the CO Cameron bands is ~0.5 kR. The IUVS dataset contains 33,319 scans from 4,314 MAVEN orbits covering 1 December 2014 through 8 May 2020. There are 278 scans containing confirmed discrete aurora detections.

2.2. Solar Wind

We use orbit-averaged solar wind properties from MAVEN's Magnetometer (MAG) and Solar Wind Ion Analyzer (SWIA), derived with the method described in Halekas et al. (2017). Using this method, averages of solar wind properties are computed for each orbit using observations obtained during the apoapsis segment of MAVENs orbit when the spacecraft was outside the Martian bow shock. SWIA provides observations of the solar wind proton density (ρ) and velocity (V_{sw}) which are used to calculate the solar wind dynamic pressure as ρV_{sw}^2. MAG provides observations of the solar wind IMF vector components which are used to calculate the IMF clock and cone angles.

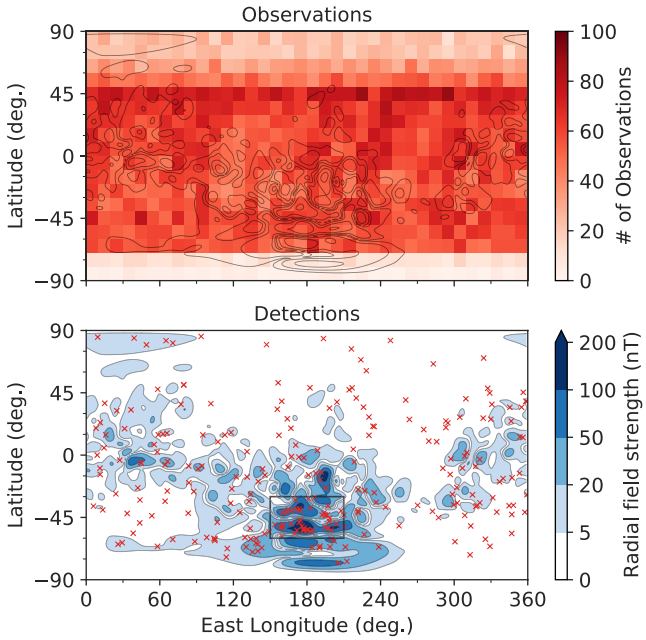

Figure 1. Observational coverage of the IUVS observations used in this study. The top panel shows number of IUVS nightside limb scans in squares spanning 10° latitude and 10° longitude. The bottom panel shows the locations of the discrete aurora detections (red x's). The rectangle outlines the "strong crustal field region". In both panels, contours of the radial crustal magnetic field strength at 400 km are shown using levels of 5 nT, 20 nT, 50 nT, 100 nT, and 200 nT (Morschhauser et al., 2014).

In Mars-Solar-Orbital (MSO) coordinates (X_{MSO} points from Mars to the Sun, Y_{MSO} points opposite Mars' orbital velocity, and Z_{MSO} is determined by the right-hand-rule), the clock angle describes the direction of the IMF projected onto the Y_{MSO}-Z_{MSO} plane. We define it as

$$\theta_{\text{clock}} = \arctan\left(B_y / B_z\right) \tag{1}$$

where B_y and B_z are the IMF components. The angle is defined such that 0° corresponds to pointing along the Z_{MSO} axis, +90° corresponds to pointing along the Y_{MSO} axis, and −90° corresponds to pointing anti-parallel to the Y_{MSO} axis. The sign of θ_{clock} is the same as the sign of the B_y component.

The IMF cone angle describes the direction of the IMF with respect to the X_{MSO} axis (the Mars-Sun line). We define the cone angle as

$$\theta_{\text{cone}} = \arccos\left(B_x / |\vec{B}|\right) \tag{2}$$

where $|\vec{B}|$ is the IMF magnitude. With this definition, 0° corresponds to pointing along the X_{MSO} axis (anti-radially from Mars toward the Sun) and 90° corresponds to an IMF perpendicular to the Mars-Sun line. Cone angles less than 90° correspond to positive B_x components while cone angles greater than 90° correspond to negative B_x components.

We wish to assign the solar wind properties to each IUVS limb scan, but there are two complications. First, MAVEN's solar wind coverage is incomplete because the spacecraft only traverses beyond the bow shock during orbits that have their apoapsis segment on the dayside. Second, the solar wind properties are obtained during apoapsis but the IUVS limb scans are conducted during periapsis, making the two measurements separated by at least a few hours. Therefore, to assign solar wind properties to a limb scan, we require the observations be separated by no more than one MAVEN orbital period (3.6–4.6 hr). Nearly all the measurements have a separation between 1.0 and 2.5 hr. This separation leads to some uncertainty in our analysis because solar wind conditions can change on shorter timescales, but is likely short enough to conduct an accurate study (Marquette et al., 2018). After assigning the solar wind properties our final dataset contains 31,308 limb scans from 3,718 MAVEN orbits covering 1 December 2014 through 1 May 2020. There are 248 scans containing confirmed discrete aurora detections that could be assigned solar wind properties.

Figure 1 (top) shows the latitude and longitude coverage of the IUVS observations (detections plus non-detections). The coverage is somewhat uniform across most latitudes but there are fewer observations in the polar regions. Figure 1 (bottom) shows the locations of the discrete aurora detections overlaid against a map of the radial crustal magnetic field strength at 400 km (Morschhauser et al., 2014). The discrete aurora are concentrated near strong radial crustal field regions, as has been discussed in previous work (Gérard et al., 2015; Leblanc et al., 2008), but also form near weak crustal field regions in smaller quantities (Schneider et al., 2021).

3. Method

With upstream solar wind properties assigned to each IUVS observation we can address our primary goal of determining how the discrete aurora detection frequency depends on upstream solar wind conditions. Our method is simple: plot histograms of the detection frequency as a function of solar wind dynamic pressure, IMF clock angle, and IMF cone angle and look for trends. The detection frequencies, f, are percentages calculated using

$$f = 100\left(\frac{D}{D+N}\right) \tag{3}$$

where D is the number of limb scans with a discrete aurora detection and N is the number of limb scans without a discrete aurora detection.

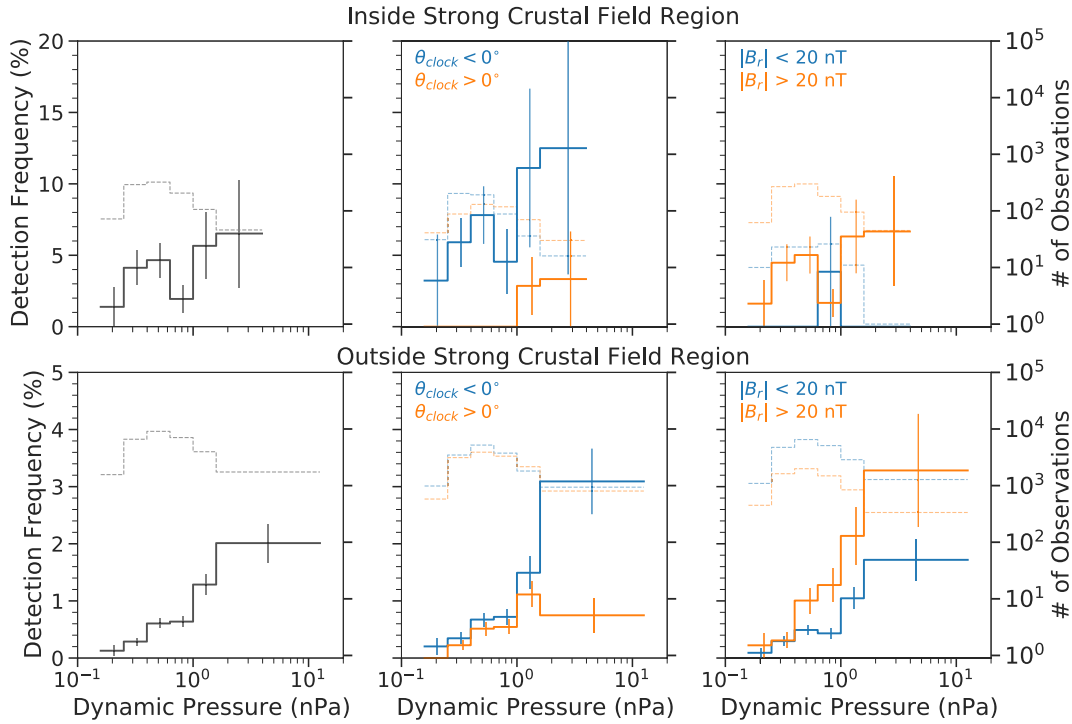

Figure 2. Discrete aurora detection frequencies as a function of solar wind dynamic pressure. The top three panels are for inside the strong crustal field region while the bottom three panels are for outside the strong crustal field region. In each panel the solid lines show the detection frequencies (left vertical axis) and the dashed lines shows the total number of observations (right vertical axis). The two left panels show all the data either inside or outside the strong crustal field region, the middle panels show data separated into categories of negative and positive IMF clock angle, and the right panels show data separated into categories of weak (<20 nT) and strong (>20 nT) radial crustal magnetic field strength. The error bars shown for each histogram are calculated using Poisson counting statistics. To make the trends more clear, the vertical axes in the top panels have different ranges than the vertical axes in the bottom panels. The highest dynamic pressure bin is wider than others to include more observations and improve the statistical significance.

We must be cautious when interpreting the detection frequency trends because multiple variables are convolved within the observations. Furthermore, the results of Schneider21 show that the detection frequency within the strongest crustal field region on Mars is highly sensitive to the IMF clock angle and that, in general, the detection frequency increases with increasing radial crustal magnetic field strength. To account for these known trends, we compute our histograms after separating the data into several subsets.

First, we separate the data based on their location with respect to the strong crustal field region (SCFR). We adopt the same method used in Schneider21: observations inside a rectangle spanning 30°S−60°S in latitude and 150°E−210°E in longitude are considered to be "inside" the SCFR and all other locations are considered to be "outside" the SCFR. Then, for each solar wind property, we compute five detection frequency histograms using data from inside the SCFR, and five detection frequency histograms using data from outside the SCFR. The first histograms are computed using all of the data in each regional subset. The next two histograms are computed after separating the regional subsets into categories of positive or negative IMF clock angle. The last two histograms are computed after separating regional subsets into categories of weak or strong radial crustal field strength. The radial crustal field strengths are determined the same way as in Schneider21, using the average radial field strength below 250 km as measured by MAVEN (T. D. Weber, 2020).

4. Results

4.1. Solar Wind Dynamic Pressure

Figure 2 shows the discrete aurora detection frequencies as a function of solar wind dynamic pressure. Histograms for aurora inside and outside the SCFR region are shown in the top and bottom rows of Figure 2, respectively. The

left two panels show the detection frequencies (solid lines) and number of observations (dashed lines) for all the data in each crustal field subset. Both inside and outside the SCFR, the number of observations histograms are consistent with the expected distribution of solar wind dynamic pressures at Mars (Marquette et al., 2018). The pressures range between 0.1 and 12.5 nPa with a mean of 0.7 nPa and a median of 0.56 nPa.

The detection frequency histograms in the left two panels of Figure 2 show that, inside the SCFR, there is a moderate correlation between the detection frequency and solar wind dynamic pressure. The detection frequency inside the SCFR increases with increase dynamic pressure but, because there are so few observations in the two highest dynamic pressure bins, the trend is not statistically robust. Outside the SCFR, however, there is statistically significant trend and the detection frequency increases monotonically with increasing dynamic pressure. The detection frequency outside the SCFR increases from 0.13(±0.09)% at low dynamic pressure (0.2 nPa) to 2.0(±0.3)% at high dynamic pressure (2–10 nPa).

Inspection of the top-middle panel in Figure 2 reveals that the trend inside the SCFR is only present for negative clock angles. This is expected given the results in Schneider21 that showed the discrete aurora in this region are observed almost exclusively at evening local times and negative clock angles. Further, as shown in the top-right panel, the trend inside the SCFR is most prominent in regions of strong radial crustal magnetic field. This is also expected given that the vast majority of observations inside the SCFR have radial crustal field strengths greater than 20 nT.

Outside the SCFR, inspection of the bottom-middle and bottom-right panels in Figure 2 reveals that the clock angle and radial field strength have some affect on the aurora detection frequency. In both panels there is a divergence between the two histograms at high dynamic pressures. This suggests that, outside the SCFR, the detection frequency is most sensitive to the dynamic pressure for negative IMF clock angles and in strong crustal field regions. In summary, these results show that the auroral detection frequency outside the SCFR is very sensitive to the solar wind dynamic pressure. Higher dynamic pressures lead to higher detection frequencies. Inside the SCFR, the detection frequency is only moderately dependent on the dynamic pressure and more observations are needed to fully determine the trend.

4.2. IMF Strength

Figure 3 shows the discrete aurora detection frequencies as a function of IMF strength using the same format as Figure 2. Inside the SCFR, the detection frequency is somewhat higher at increased IMF strengths but the trend is not monotonic nor particularly robust. Outside the SCFR, the trend is more convincing with the detection frequency increasing monotonically with increasing IMF strength, from 0.32(±0.14)% at the lowest IMF strengths (0.75 nT) to 1.2(±0.17)% at the highest IMF strengths (3–8 nT).

We must be cautious when interpreting this trend because there is a strong positive correlation between the IMF strength and dynamic pressure. In our solar wind data, the Pearson correlation coefficient between the IMF strength and dynamic pressure is 0.49, making it difficult to isolate the effects of the two parameters on the aurora detection frequency. Nonetheless, we can gain confidence that the dynamic pressure is the dominant controlling parameter through inspection of Figure 4, which shows the detection frequency as a function of IMF strength for fixed dynamic pressure levels (left panel), and the detection frequency as a function of dynamic pressure for fixed IMF strengths (right panel). The left panel shows the trends in detection frequency with IMF strength are weak at all three dynamic pressure levels. Alternatively, the right panel shows the trends in detection frequency with dynamic pressure are strong at all three IMF strength levels. This demonstrates that the dynamic pressure is more of a controlling factor than the IMF strength outside the SCFR.

4.3. IMF Cone Angle

Figure 5 shows the detection frequencies as a function of IMF cone angle. The most striking feature inside the SCFR is the lack of any detections at cone angles less than 30°. This suggests discrete aurora inside the SCFR are unlikely to occur when the IMF is pointing from Mars toward the Sun along the X_{MSO} axis (anti-radially). Interestingly, the same is not true for cone angles near 180° when IMF is pointing in the opposite direction. Instead, the detection frequency drops significantly for near-radial cone angles between 120° and 150°.

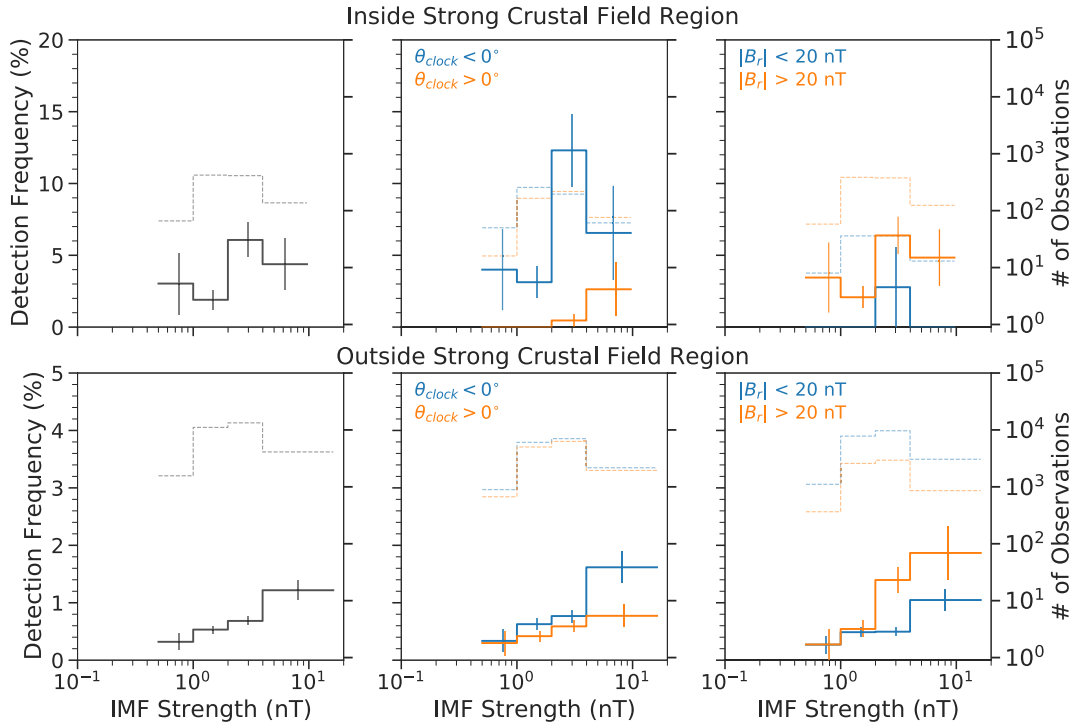

Figure 3. Similar to Figure 2 but showing detection frequency as a function of IMF strength.

Outside the SCFR there is no strong trend in the detection frequency as a function of IMF cone angle, although the detection frequency is smaller for cone angles between 120° and 150° at locations where the radial field strength exceeds 20 nT. These results show that the detection frequency is only weakly dependent on the IMF cone angle, especially in regions of weak radial crustal magnetic field.

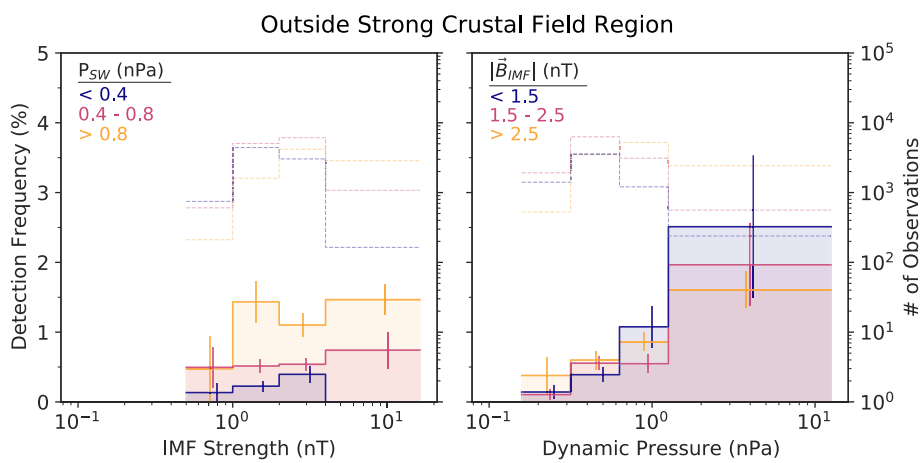

Figure 4. The left panel shows the discrete aurora detection frequencies as a function of IMF strength for fixed solar wind dynamic pressure bins of <0.4 nPa, 0.4–0.8 nPa, and >0.8 nPa. The right panel shows the detection frequencies as a function of solar wind dynamic pressure for fixed IMF strength bins of <1.5 nT, 1.5–2.5 nT, and >2.5 nT. Error bars are calculated using Poisson counting statistics.

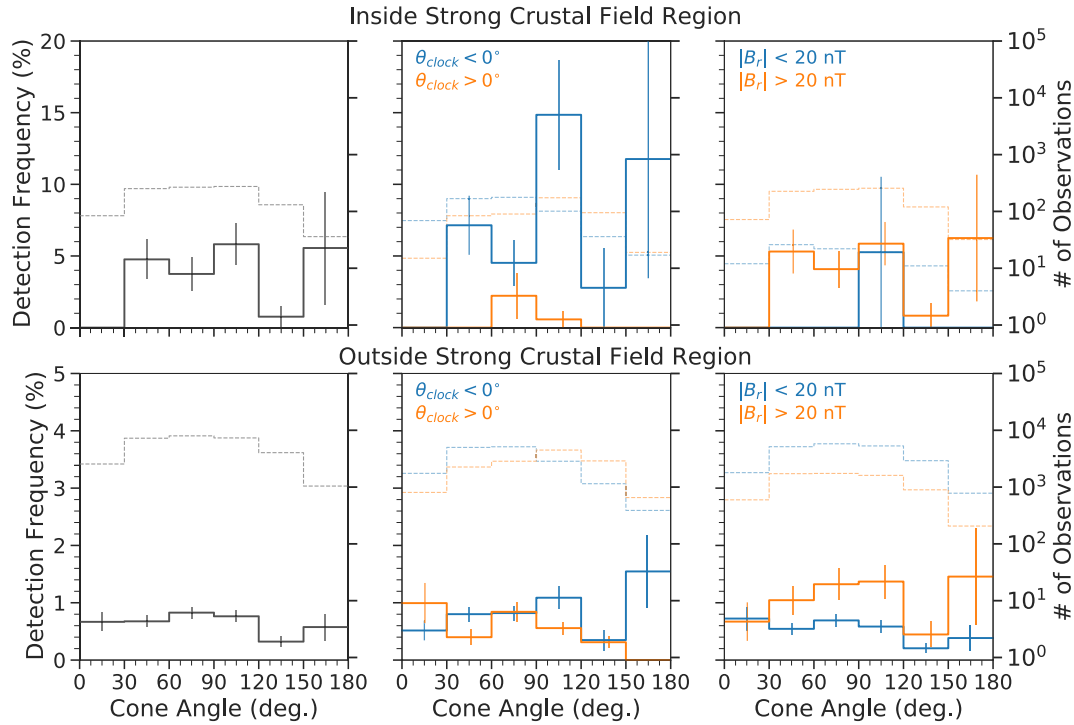

Figure 5. Similar to Figure 2 but showing detection frequency as a function of IMF cone angle.

5. Discussion and Conclusions

Table 1 summarizes how solar wind conditions qualitatively affect the discrete aurora detection frequency inside and outside the SCFR. For each region, the extent in which the detection frequency depends on each solar wind parameter is described as either "weak", "moderate", or "strong". One caveat to keep in mind when interpreting the results is that our derived detection frequencies are based on IUVS nightside limb scans, which have a detection threshold brightness of ~0.5 kR in the CO Cameron bands (Schneider et al., 2021). This adds some uncertainty to our results since some limb scans may contain aurora that are too dim to be detected.

Our most conclusive finding is that, outside the SCFR, the detection frequency is strongly dependent on the solar wind dynamic pressure. The detection frequency increases nearly monotonically as the solar wind dynamic pressure increases. This finding is consistent with previous work showing that high solar wind dynamic pressures increase the percentage of open magnetic field lines on the nightside (D. A. Brain et al., 2020; T. Weber et al., 2020) and lead to higher electron precipitation rates (Lillis & Brain, 2013; Lillis et al., 2018). It also suggests that discrete aurora are more common during transient space weather events such as interplanetary coronal mass ejections (ICMEs), stream interaction regions (SIRs), and corotating interaction regions (CIRs), which are accompanied by sudden increases in the dynamic pressure (Allen et al., 2021; Lee et al., 2010, 2017). Recent modeling work by Fang et al. (2022) also predicts that discrete aurora should be more common during ICMEs. Alternatively, inside the SCFR, the detection frequency is primarily controlled by the orientation of the IMF, being most sensitive to the IMF clock angle.

Figure 6 shows the auroral emission brightness as a function of radial crustal field strength (left) and solar wind dynamic pressure (right). The left panel shows the emission brightness increases with radial field strength, confirming what was previously shown in Figure 8 of Schneider21. Interestingly, though, the right panel shows the emission brightness is insensitive to the dynamic pressure. Hence, increased dynamic pressures result in more aurora across the planet, but do not lead to brighter aurora. This suggests the energy

Table 1
Summary of How the Discrete Aurora Detection Frequency Depends on Different Solar Wind Properties Both Inside and Outside the Strong Crustal Field Region (SCFR)

	Inside SCFR	Outside SCFR
Dynamic Pressure	Moderate	Strong
IMF Strength	Moderate	Moderate
Cone Angle	Moderate[a]	Weak
Clock Angle[b]	Strong	Weak

Note. For each solar wind parameter, the dependence is qualitatively described as either "weak", "moderate", or "strong".

[a]Few detections when the clock angle is <30° or 120°–150°. [b]Clock angle results first reported in Schneider et al. (2021).

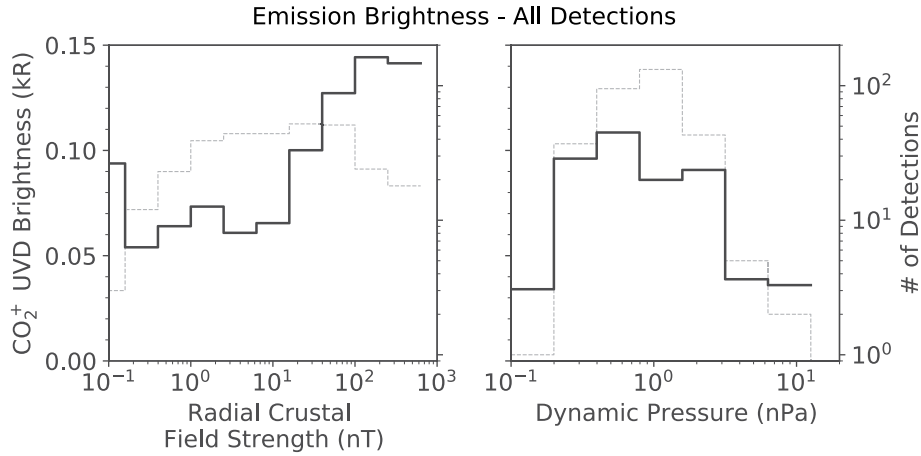

Figure 6. Discrete aurora CO_2^+ ultraviolet doublet emission brightness as a function of radial crustal field strength (left) and solar wind dynamic pressure (right). In each panel the solid lines show the emission brightness (left vertical axis) and the dashed lines show the number of detections (right vertical axis).

flux of the auroral electrons does not increase with solar wind dynamic pressure. Again this is consistent with the interpretation that more aurora are observed during high dynamic pressures because there is a higher fraction of open field topology and expanded magnetic cusp regions (T. Weber et al., 2019).

Our results also show that the detection frequency inside the SCFR has an interesting IMF cone angle dependence, with few aurora observed at cone angles less than 30° or between 120° and 150°. The detection frequency in this region also has a strong clock angle and local time dependence, with aurora occurring almost exclusively at evening local times and negative clock angles (Schneider21). Both of these findings point to the importance of the IMF orientation—which affects the magnetic field draping pattern (Fang et al., 2018) and low-altitude magnetic topology (T. Weber et al., 2020)—in controlling the formation of discrete aurora in the SCFR. Positive clock angles and cone angles less than 30° or between 120° and 150° appear to make conditions unfavorable for magnetic reconnection or particle acceleration in the SCFR.

Finally, it is interesting that outside the SCFR the aurora detection frequency has a much weaker dependence on the IMF clock and cone angles. The weaker crustal fields in this region appear to make the IMF orientation a less important factor in determining aurora formation. Instead, the aurora outside the SCFR are primarily controlled by the solar wind dynamic pressure.

In conclusion, our results presented here reveal new aspects in regards to how upstream solar wind conditions affect the formation of discrete aurora at Mars. These new constraints on the aurora detection frequency with upstream solar wind conditions will be useful for future theoretical and modeling studies that attempt to unveil the physics and formation mechanisms of discrete aurora at Mars.

Data Availability Statement

All of the MAVEN solar wind data used in this study are publicly available from the Planetary Data System (https://pds-ppi.igpp.ucla.edu/search/?sc=MAVEN&t=Mars). As described in Schneider et al. (2021), the IUVS limb scan data used in this work (Jain & Schneider, 2021) is publicly archived on the FAIR-compliant CU Scholar Repository at https://doi.org/10.25810/2a0h-9w11.

Acknowledgments
This research was conducted under the support of the MAVEN mission which is funded by NASA headquarters. X. Fang was supported by NASA Grant 80NSSC19K0562. J.-C. Gérard and L. Soret acknowledge funding from BELSPO, with financial and contractual coordination by the ESA PRODEX Office (PEA Grant No. 4000121493). The authors thank Dave Brain, Janet Luhmann, and Dave Mitchell for providing useful insights.

References

Akbari, H., Andersson, L., Fowler, C., & Mitchell, D. (2019). Spectral analysis of accelerated electron populations at Mars. *Journal of Geophysical Research: Space Physics*, *124*(10), 8056–8065. https://doi.org/10.1029/2019JA026738

Allen, R. C., Ho, G. C., Jian, L. K., Vines, S. K., Bale, S. D., Case, A. W., et al. (2021). A living catalog of stream interaction regions in the Parker Solar Probe era. *Astronomy & Astrophysics*, *650*, A25. https://doi.org/10.1051/0004-6361/202039833

Bertaux, J.-L., Korablev, O., Perrier, S., Quémerais, E., Montmessin, F., Leblanc, F., et al. (2006). SPICAM on Mars Express: Observing modes and overview of UV spectrometer data and scientific results. *Journal of Geophysical Research*, *111*(E10), 1–40. https://doi.org/10.1029/2006JE002690

Bertaux, J.-L., Leblanc, F., Witasse, O., Quemerais, E., Lilensten, J., Stern, S. A., et al. (2005). Discovery of an aurora on Mars. *Nature*, *435*(7043), 790–794. https://doi.org/10.1038/nature03603

Birn, J., Artemyev, A. V., Baker, D. N., Echim, M., Hoshino, M., & Zelenyi, L. M. (2012). Particle acceleration in the magnetotail and aurora. *Space Science Reviews*, *173*(1–4), 49–102. https://doi.org/10.1007/s11214-012-9874-4

Brain, D., & Halekas, J. S. (2013). Aurora in Martian mini magnetospheres. In A. Keiling, E. Donovan, F. Bagenal, & T. Karlsson (Eds.), *Geophysical monograph series* (pp. 123–132). American Geophysical Union. https://doi.org/10.1029/2011GM001201

Brain, D. A., Halekas, J. S., Peticolas, L. M., Lin, R. P., Luhmann, J. G., Mitchell, D. L., et al. (2006). On the origin of aurorae on Mars. *Geophysical Research Letters*, *33*(1). https://doi.org/10.1029/2005GL024782

Brain, D. A., Weber, T., Xu, S., Mitchell, D. L., Lillis, R. J., Halekas, J. S., et al. (2020). Variations in nightside magnetic field topology at Mars. *Geophysical Research Letters*, *47*, e2020GL088921. https://doi.org/10.1029/2020GL088921

Deighan, J., Jain, S. K., Chaffin, M. S., Fang, X., Halekas, J. S., Clarke, J. T., et al. (2018). Discovery of a proton aurora at Mars. *Nature Astronomy*, *2*(10), 802–807. https://doi.org/10.1038/s41550-018-0538-5

Fang, X., Ma, Y., Luhmann, J., Dong, Y., Brain, D., Hurley, D., et al. (2018). The morphology of the solar wind magnetic field draping on the dayside of Mars and its variability. *Geophysical Research Letters*, *45*(8), 3356–3365. https://doi.org/10.1002/2018GL077230

Fang, X., Ma, Y., Schneider, N., Girazian, Z., Luhmann, J., Milby, Z., et al. (2022). Discrete aurora on the nightside of Mars: Occurrence location and probability. *Journal of Geophysical Research: Space Physics*, *127*, e2021JA029716. https://doi.org/10.1029/2021JA029716

Gérard, J.-C., Soret, L., Libert, L., Lundin, R., Stiepen, A., Radioti, A., & Bertaux, J.-L. (2015). Concurrent observations of ultraviolet aurora and energetic electron precipitation with Mars Express. *Journal of Geophysical Research: Space Physics*, *120*(8), 6749–6765. https://doi.org/10.1002/2015JA021150

Halekas, J. S., Ruhunusiri, S., Harada, Y., Collinson, G., Mitchell, D. L., Mazelle, C., et al. (2017). Structure, dynamics, and seasonal variability of the Mars-solar wind interaction: MAVEN solar wind Ion Analyzer in-flight performance and science results. *Journal of Geophysical Research: Space Physics*, *122*(1), 547–578. https://doi.org/10.1002/2016JA023167

Hughes, A., Chaffin, M., Mierkiewicz, E., Deighan, J., Jain, S., Schneider, N., et al. (2019). Proton aurora on Mars: A dayside Phenomenon Pervasive in southern summer. *Journal of Geophysical Research: Space Physics*, *124*(12), 10533–10548. https://doi.org/10.1029/2019JA027140

Jain, S., Schneider, N. M. (2021). Discrete aurora on Mars: Insights into their distribution and activity from MAVEN/IUVS observations [data set]. University of Colorado Boulder. https://doi.org/10.25810/2A0H-9W11

Leblanc, F., Witasse, O., Lilensten, J., Frahm, R. A., Safaenili, A., Brain, D. A., et al. (2008). Observations of aurorae by SPICAM ultraviolet spectrograph on board Mars Express: Simultaneous ASPERA-3 and MARSIS measurements. *Journal of Geophysical Research*, *113*(A8). https://doi.org/10.1029/2008JA013033

Leblanc, F., Witasse, O., Winningham, J., Brain, D., Lilensten, J., Blelly, P.-L., et al. (2006). Origins of the Martian aurora observed by spectroscopy for Investigation of characteristics of the atmosphere of Mars (SPICAM) on board Mars express. *Journal of Geophysical Research*, *111*(A9). https://doi.org/10.1029/2006JA011763

Lee, C. O., Hara, T., Halekas, J. S., Thiemann, E., Chamberlin, P., Eparvier, F., et al. (2017). MAVEN observations of the solar cycle 24 space weather conditions at Mars. *Journal of Geophysical Research: Space Physics*, *122*, 2768–2794. https://doi.org/10.1002/2016JA023495

Lee, C. O., Luhmann, J. G., de Pater, I., Mason, G. M., Haggerty, D., Richardson, I. G., et al. (2010). Organization of energetic particles by the solar wind structure during the declining to minimum phase of solar cycle 23. *Solar Physics*, *263*(1), 239–261. https://doi.org/10.1007/s11207-010-9556-x

Lillis, R. J., & Brain, D. A. (2013). Nightside electron precipitation at Mars: Geographic variability and dependence on solar wind conditions. *Journal of Geophysical Research*, *118*, 3546–3556. https://doi.org/10.1002/jgra.50171

Lillis, R. J., Mitchell, D. L., Steckiewicz, M., Brain, D., Xu, S., Weber, T., et al. (2018). Ionizing electrons on the Martian nightside: Structure and variability. *Journal of Geophysical Research: Space Physics*, *123*(5), 4349–4363. https://doi.org/10.1029/2017JA025151

Marquette, M. L., Lillis, R. J., Halekas, J. S., Luhmann, J. G., Gruesbeck, J. R., & Espley, J. R. (2018). Autocorrelation study of solar wind Plasma and IMF properties as measured by the MAVEN spacecraft. *Journal of Geophysical Research: Space Physics*, *123*(4), 2493–2512. https://doi.org/10.1002/2018JA025209

McClintock, W. E., Schneider, N. M., Holsclaw, G. M., Clarke, J. T., Hoskins, A. C., Stewart, I., et al. (2015). The imaging ultraviolet spectrograph (IUVS) for the MAVEN mission. *Space Science Reviews*, *195*(1–4), 75–124. https://doi.org/10.1007/s11214-014-0098-7

Morschhauser, A., Lesur, V., & Grott, M. (2014). A spherical harmonic model of the lithospheric magnetic field of Mars. *Journal of Geophysical Research: Planets*, *119*(6), 1162–1188. https://doi.org/10.1002/2013JE004555

Ritter, B., Gérard, J.-C., Hubert, B., Rodriguez, L., & Montmessin, F. (2018). Observations of the proton aurora on Mars with SPICAM on board Mars Express. *Geophysical Research Letters*, *45*(2), 612–619. https://doi.org/10.1002/2017GL076235

Schneider, N. M., Deighan, J. I., Jain, S. K., Stiepen, A., Stewart, A. I. F., Larson, D., et al. (2015). Discovery of diffuse aurora on Mars. *Science*, *350*(6261). https://doi.org/10.1126/science.aad0313

Schneider, N. M., Milby, Z., Jain, S. K., Gérard, J.-C., Soret, L., Brain, D. A., et al. (2021). Discrete aurora on Mars: Insights into their distribution and activity from MAVEN/IUVS observations. *Journal of Geophysical Research: Space Physics*, *126*(10), e2021JA029428. https://doi.org/10.1029/2021JA029428

Soret, L., Gérard, J.-C., Libert, L., Shematovich, V. I., Bisikalo, D. V., Stiepen, A., & Bertaux, J.-L. (2016). SPICAM observations and modeling of Mars aurorae. *Icarus*, *264*, 398–406. https://doi.org/10.1016/j.icarus.2015.09.023

Soret, L., Gérard, J.-C., Schneider, N., Jain, S., Milby, Z., Ritter, B., et al. (2021). Discrete Aurora on Mars: Spectral properties, vertical profiles, and electron energies. *Journal of Geophysical Research: Space Physics*, *126*(10), e2021JA029495. https://doi.org/10.1029/2021JA029495

Weber, T., Brain, D., Mitchell, D., Xu, S., Espley, J., Halekas, J., et al. (2019). The influence of solar wind pressure on Martian crustal magnetic field topology. *Geophysical Research Letters*, *46*, 2347–2354. https://doi.org/10.1029/2019GL081913

Weber, T., Brain, D., Xu, S., Mitchell, D., Espley, J., Halekas, J., et al. (2020). The influence of interplanetary magnetic field direction on Martian Crustal Magnetic Field Topology. *Geophysical Research Letters*, *47*(19), e2020GL087757. https://doi.org/10.1029/2020GL087757

Weber, T. D. (2020). *The role of crustal magnetic fields in atmospheric escape from Mars*. Ph.D., University of Colorado at Boulder (ISBN: 9798557022927).

Xu, S., Mitchell, D. L., McFadden, J. P., Fillingim, M. O., Andersson, L., Brain, D. A., et al. (2020). Inverted-V electron acceleration events concurring with localized auroral observations at Mars by MAVEN. *Geophysical Research Letters*, *47*, e2020GL087414. https://doi.org/10.1029/2020GL087414